Research Square

Preprints are preliminary reports that have not undergone peer review.
They should not be considered conclusive, used to inform clinical practice,
or referenced by the media as validated information.

Photocatalytic Conversion of Volatile Fatty Acids into H_2 and C 1 –C 6 Alkanes over Cu 2 O/BiPO 4 p-n Heterojunctions: Insights into Radical Intermediate Coupling

Qingtao Chen
Zhengzhou University of Light Industry
Xiangdong Shi
Luohe Vocational Technology College
Xianghai Rao
Zhengzhou University of Light Industry
Mingyang Zhu
Luohe Vocational Technology College
Xiaoyun Qin
Zhengzhou University of Light Industry
Dan Luo
Beijing Institute of Nanoenergy and Nanosystems
Fenghua Chen
phenix@zzuli.edu.cn

Zhengzhou University of Light Industry

Research Article

Keywords: Cu2O, BiPO4, Photocatalytic H2 and hydrocarbon production, Volatile fatty acids, Biomass valorization

Posted Date: October 29th, 2026

DOI: https://doi.org/10.21203/rs.3.rs-11258650/v1

License: This work is licensed under a Creative Commons Attribution 4.0 International License.
Read Full License

Additional Declarations: No competing interests reported.

Abstract

Photocatalytic conversion of biomass-derived volatile fatty acids (VFAs) into H_2 and hydrocarbons remains challenging, largely because the product distribution is governed by the selective coupling of alkyl radical intermediates generated via the photo-Kolbe reaction. Herein, we synthesized a series of $Cu_2O/BiPO_4$ p-n heterojunction composites with varying Cu_2O loadings (1–15 wt%) and evaluated their performance for converting acetic (HAc), propionic (HPr), and butyric acid (HBu) into H_2 and C_1–C_6 alkanes under UV irradiation. The p-n heterojunction is proposed to facilitate charge separation and to influence the oxidative power of photogenerated holes, thereby affecting the decarboxylation of carboxylates to generate alkyl radical intermediates ($\cdot CH_3$, $\cdot CH_2CH_3$, $\cdot CH_2CH_2CH_3$), whose subsequent coupling pathways dictate the product selectivity. The optimized CBP-9 (9 wt% Cu_2O) delivered a 2.49-fold higher total H_2/alkane yield than pristine $BiPO_4$ from HAc, with 85.71% total organic carbon removal within 4 h. For HPr and HBu, the yields of ethane/butane and methane/propane were enhanced by 2.27- and 1.67-fold, respectively. Mechanistic studies based on photoluminescence, transient photocurrent, and electrochemical impedance spectroscopy indicate that the p-n junction promotes spatial charge separation and improves stability. The catalyst retained > 85% of its initial activity after five cycles. This work provides insights into radical intermediate coupling in the photocatalytic conversion of VFAs over $Cu_2O/BiPO_4$ heterojunctions, demonstrating the potential for directly converting wet biomass residues into H_2-enriched fuel gases.

1 Introduction

Energy resource shortage and environmental pollution have driven the search for clean and renewable fuels [1,2]. Hydrogen and hydrocarbons are regarded as promising future fuels, but their production still relies heavily on fossil resources. Photocatalytic conversion of biomass-derived feedstocks into H_2 and hydrocarbons offers a sustainable alternative [3–5]. Among various biomass-derived substrates, volatile fatty acids (VFAs) are particularly attractive because they are widely generated as byproducts during fermentative biomass conversion and can serve as electron donors in photocatalytic systems, enabling simultaneous wastewater treatment and fuel production [6,7]. However, the photocatalytic conversion of VFAs into H_2 and hydrocarbons is a complex process in which the product distribution is governed by the selective coupling of alkyl radical intermediates generated via the photo-Kolbe reaction [8,9]. Understanding and controlling this radical intermediate chemistry remains a significant challenge.

Bismuth phosphate ($BiPO_4$) is an n-type semiconductor with a wide band gap (Eg = 4.16 eV) and has been widely studied for pollutant degradation [10,11]. However, its rapid charge recombination limits its photocatalytic efficiency [12–14]. Coupling $BiPO_4$ with a p-type semiconductor to form a heterojunction is an effective strategy to promote charge separation and extend spectral absorption [15–17]. Cuprous oxide (Cu_2O) is a p-type semiconductor with a narrow band gap (Eg = 2.0 eV) and strong visible-light absorption [18,19], but it suffers from photo-corrosion when used alone [20]. Coupling Cu_2O with an appropriate support can mitigate this issue and enhance activity [21–23]. In a $Cu_2O/BiPO_4$ p-n

heterojunction, the built-in electric field can drive photogenerated electrons and holes in opposite directions, suppressing recombination. More importantly, the band alignment may also modulate the oxidative power of photogenerated holes, thereby influencing the decarboxylation of carboxylates and the subsequent coupling of alkyl radical intermediates. Liu et al. [24] and Li et al. [25] reported $Cu_2O/BiPO_4$ composites for pollutant degradation and demonstrated enhanced charge separation. However, these studies focused on degradation, and the radical intermediate chemistry underlying VFA conversion over $Cu_2O/BiPO_4$ heterojunctions remains largely unexplored.

Biomass is an abundant, low-cost, and renewable resource for sustainable fuel production [26]. During fermentative biomass conversion, large amounts of volatile fatty acids (VFAs) are generated as byproducts [27]. Photocatalytic conversion of VFAs into H_2 and hydrocarbons not only valorizes these waste streams but also enables simultaneous wastewater treatment and energy recovery [28,29]. In photocatalytic VFA conversion, carboxylates undergo the photo-Kolbe reaction, in which photogenerated holes oxidize $RCOO^-$ to alkyl radicals (·R) and CO_2 [30,31]. The subsequent coupling of these radical intermediates dictates the product distribution: $\cdot R + \cdot H \rightarrow RH$, $\cdot R + \cdot R \rightarrow R–R$, and $\cdot R + \cdot OH \rightarrow ROH$ (Hofer-Moest reaction) [32,33]. Since HAc, HPr, and HBu have different carbon chain lengths, they generate distinct radicals ($\cdot CH_3$, $\cdot CH_2CH_3$, and $\cdot CH_2CH_2CH_3$), leading to different C_1–C_6 alkane distributions [34–36]. However, how the $Cu_2O/BiPO_4$ heterojunction influences the generation and coupling of these radical intermediates remains unclear. In this work, we aim to provide insights into the radical intermediate coupling chemistry in the photocatalytic conversion of VFAs over $Cu_2O/BiPO_4$ p-n heterojunctions. The product distribution is correlated with the type of alkyl radical generated from each VFA, and the role of the heterojunction in charge separation and interfacial chemistry is discussed based on photoluminescence, transient photocurrent, electrochemical impedance spectroscopy, and XPS results. The findings may contribute to a better understanding of how heterojunction interfacial properties influence radical intermediate coupling and product selectivity in photocatalytic biomass valorization.

2 Results and Discussion

2.1 Structure and Morphology Analysis

The morphologies and particle sizes of as-synthesized samples were illustrated in Fig. 1. As shown in Fig. 1a, it was observed that the pure $BiPO_4$ particles were present as larger cuboids and smaller rods together. The larger cuboid-like $BiPO_4$ particles had the length of 1.5 μm and the width of 1μm. While, the small rod-like $BiPO_4$ particles were about 1.0 μm long and 200 nm wide. According to Fig. 1b, the prepared Cu_2O particles under our conditions were composed of uniform nanospheres with a diameter of about 300 nm. However, for the CBP-9 sample (Fig. 1c), it could be easily seen that smaller Cu_2O nanospheres were irregularly loaded on surfaces of both cuboids $BiPO_4$ or rods $BiPO_4$, respectively. The above results verified that Cu_2O was indeed present in $Cu_2O/BiPO_4$ composites. A further deep

observation of the CBP-9 samples was performed by TEM and HRTEM, respectively. It could be clearly seen from Fig. 1d and Fig. 1e that some Cu_2O nanoparticles were uniformly adhered to the smooth surface of $BiPO_4$ rods. The interlayer distance in Fig. 2e was determined as 0.256 nm, corresponding to the (-202) plane of the monoclinic $BiPO_4$. Similarly, the interplanar spacing in Fig. 2e was measured as 0.239 nm, corresponding to the (111) plane of cubic Cu_2O sphere. In addition, from the TEM-mapping spectra of CBP-9 (Fig. 1f), it was obviously indicated that Cu, O, P and Bi elements could be found in $Cu_2O/BiPO_4$ composites. From above observations, the Cu_2O spheres were tightly adhered on the surface with $BiPO_4$ rods in the CBP-9 sample, indicating the successful formation of the $Cu_2O/BiPO_4$ composites.

The crystal structures of as-prepared pure Cu_2O, pure $BiPO_4$ and $Cu_2O/BiPO_4$ composites were studied by XRD analysis (Fig. 2). According to Fig. 2a, the typical diffraction peaks of the pure Cu_2O could be well indexed as cubic Cu_2O (JCPDS 65-3288) and no other diffraction peaks for impurities could be identified. On the other hand, the characteristic diffraction peaks for the pure $BiPO_4$ could be assigned to monoclinic $BiPO_4$ (JCPDS 89–0287). For all $Cu_2O/BiPO_4$ composites, the diffraction patterns were found to be similar to that of pure $BiPO_4$, indicating that almost no obvious changes for crystal structure of $BiPO_4$ could be observed when a certain amount of Cu_2O was loaded on $BiPO_4$. However, no evidences for Cu_2O presence in XRD patterns of $Cu_2O/BiPO_4$ composites could be detected. The reason for this may be that the amount of Cu_2O was too low for well dispersed on the $BiPO_4$ particles or the crystallinity of Cu_2O was very poor. Similar phenomena have been reported when a small amount of Cu_2O loaded on other photocatalysts [37,38]. Evidence for Cu_2O presence in composites could be well proved by other characterizations.

To investigate the detailed surface elemental compositions and oxidation states of the CBP-9 sample, XPS measurements were performed, and the results were shown in Fig. 2. In Fig. 2b, the distinct peaks at various binding energies can be assigned to P 2p, Bi 4f, O 1s, and Cu 2p, respectively. These results indicated that the CBP-9 sample contained at least the P, Bi, O, and Cu elements. The chemical compositions determined by XPS analysis were consistent with those obtained from previous EDS spectra. Furthermore, the high-resolution XPS spectra were acquired to identify the different oxidation states of the elements in the CBP-9 sample. The high-resolution XPS spectrum of Bi 4f for the CBP-9 sample was presented in Fig. 2c. Instead of the expected single spin-orbit doublet for Bi^{3+}, the spectrum revealed two distinct doublets. The primary doublet, located at 159.6 eV (Bi $4f_{7/2}$) and 164.9 eV (Bi $4f_{5/2}$), was characteristic of Bi^{3+} in the $BiPO_4$ lattice, confirming the chemical integrity of the bismuth phosphate phase. However, an additional doublet appeared at 161.7 eV and 166.5 eV. At first glance, this might be misinterpreted as a secondary Bi species. Nevertheless, such a 2.1 eV positive shift (from 159.6 to 161.7 eV) was chemically implausible for bismuth reduction or oxidation under CBP-9 formation, the assignment of these peaks to a distinct Bi chemical state was excluded. Instead, we attributed this secondary doublet to Auger interference originating from the Cu_2O component. Specifically, the binding energy of the secondary doublet matched well with the Cu $M_{2,3}$ VV Auger

transitions, which were known to exhibit a characteristic doublet structure for Cu_2O [39]. Therefore, the Bi 4f core-level spectrum indicated that bismuth retained solely its + 3-oxidation state. According to Fig. 2d, the high-resolution XPS spectrum of Cu 2p for the CBP-9 exhibited a complex structure consisting of six distinct peaks, which could be deconvoluted into two spin-orbit doublets accompanied by strong shake-up satellites. Specifically, the main doublet at 932.3 eV (Cu $2p_{3/2}$) and 952.1 eV (Cu $2p_{1/2}$) was characteristic of Cu^+ in Cu_2O phase. The additional doublet at higher binding energies, namely 934.1 eV (Cu $2p_{3/2}$) and 953.8 eV (Cu $2p_{1/2}$), along with the pronounced shake-up satellite peaks at 940.7 eV and 943.8 eV, unambiguously confirmed the presence of Cu^{2+} species (CuO). The characteristic shake-up satellites, arising from the $3d^9$ configuration of Cu^{2+}, served as a definitive fingerprint for the divalent copper state. This indicated that there was a small amount of Cu^{2+} species imbedded in Cu_2O precipitate could not be completely reduced to Cu^+ species during preparation of $Cu_2O/BiPO_4$. The deconvoluted O1s spectrum in CBP-9 (Fig. 2e) was comprised of peaks corresponding to the lattice oxygen species in the PO_4^{3-} groups of $BiPO_4$ and the Cu-O bonds of Cu_2O (530.7 eV), surface hydroxyl groups (-OH) or oxygen vacancies (531.7 eV), and adsorbed molecular water (H_2O) or surface-adsorbed oxygen-containing species (533.9 eV). The high-resolution XPS spectrum of P 2p for the CBP-9 presented in Fig. 2f exhibited three distinct peaks, which can be deconvoluted into one spin-orbit doublet and an additional high-binding-energy component. The doublet at 132.8 eV (P $2p_{3/2}$) and 133.6 eV (P $2p_{1/2}$) corresponded to the PO_4^{3-} species within the $BiPO_4$ lattice. The appearance of the additional P 2p peak at 135.5 eV, which was approximately 2.7 eV higher than the main PO_4^{3-} doublet, suggests the possibility of chemical interaction between $BiPO_4$ and Cu_2O beyond a simple physical mixture. This high-binding-energy component was tentatively attributed to phosphate species that are chemically bonded to copper ions (Cu^+ or Cu^{2+}) at the interface. Specifically, some of the phosphate groups from $BiPO_4$ may coordinate with copper atoms on the Cu_2O surface, tentatively attributed to phosphate species interacting with copper ions at the interface, possibly forming P–O–Cu linkages. The formation of such interfacial bonds altered the local chemical environment of phosphorus atoms by withdrawing electron density through the bridging oxygen atom, leading to an increased binding energy in the P 2p core level spectrum. Such interfacial interaction was expected to facilitate charge transfer across the heterojunction and may play a crucial role in enhancing the separation of photogenerated electron-hole pairs in the p-n heterojunction.

The optical properties of $Cu_2O/BiPO_4$ composites were explored by UV-vis diffuse reflection spectra using pure Cu_2O and pure $BiPO_4$ as contrasts (Fig. 2). As shown in Fig. 2g, the absorption edge of pure $BiPO_4$ was about 320 nm corresponding to a ultraviolet absorption band, similar to former reported value [40]. It can be seen that the pure $BiPO_4$ showed intense absorption at wavelength from 200 to 300 nm and nearly no absorption at wavelength from 300 nm to 800 nm. For comparison, pure Cu_2O had a strong absorption at both UV region (200–400 nm) and visible region (400–680 nm). Compared with pure $BiPO_4$, all $Cu_2O/BiPO_4$ composites exhibited a considerable enhancement in light absorption at both UV region (200–400 nm) and visible light region (400–650 nm). In terms of light harvesting ability at

wavelength from 300 to 650 nm, all $Cu_2O/BiPO_4$ composites can be put in the following order: CBP-1 < CBP-3 ≈ CBP-7 < CBP-5 < CBP-10 < CBP-9 < CBP-15. The light harvesting ability of a photocatalyst was usually related to its photocatalytic activity and thus photocatalytic performances of all $Cu_2O/BiPO_4$ composites nearly followed the same order except CBP-7 and CBP-10.

The photocatalytic property of a photocatalyst is determined by its electronic structure which contained a conduction band, a valence band and a bandgap (energy difference between conduction band and valence band). The bandgap of a photocatalyst is usually calculated using Kubelka-Munk function. The Kubelka-Munk function can be written as following equation: $(\alpha hv)^2 = A(hv\text{-}E_g)^{1/2}$, where α, v, h, E_g and A stand for absorption coefficient, light frequency, Planck's constant, band gap energy and another constant, respectively. $(\alpha hv)^2$ is plotted against (hv) and illustrated in Fig. 2h. For pure $BiPO_4$, the band gap was determined to be 4.21 eV, which was somewhat higher than reported value [41]. By contrast, the band gap for pure Cu_2O was estimated about 2.20 eV, which was close to reported value [42]. However, the bandgap for CBP-9 was measured to be 2.62 eV, which was much smaller than that of $BiPO_4$, indicating that the introduction of Cu_2O significantly reduced the band gap of $BiPO_4$. As a result, the light absorption capability of the composite in the visible region was greatly enhanced. This also indirectly suggested the presence of strong electronic coupling or the formation of a p-n heterojunction structure between $BiPO_4$ and Cu_2O. The built-in electric field formed at the interface can facilitate the effective separation of photogenerated charge carriers.

The specific surface area and pore structure of the $Cu_2O/BiPO_4$ composite were evaluated through nitrogen adsorption-desorption tests. In Fig. 2i, the isotherms of the as-prepared materials showed a type IV with a H3 hysteresis loop, indicating the existence of mesoporous features. The specific surface area of $Cu_2O/BiPO_4$ was 4.5079 $m^2 \cdot g^{-1}$, which may expose more active sites, making it easier for the materials to come into contact with reactants. In the embedded diagram of Fig. 2i, the pore diameter distributions of the $Cu_2O/BiPO_4$ presented pore size distribution of mesopores with small (< 20 nm) diameters. The above characteristics suggest that $Cu_2O/BiPO_4$ is expected to have good catalytic activity.

2.2 Photocatalytic performances for production of H_2 and hydrocarbons

The photocatalytic reaction for producing hydrocarbons and H_2 over a photocatalyst is a very complex process, which is usually influenced by many factors, such as the type of photocatalyst, the type of electron donor, the pH value of the solution, the intensity of the light source, and so on. To improve the separation efficiency of photoinduced electrons and holes, various organic compounds are widely used as electron donors in photocatalytic systems. Previously, the photocatalytic performance of $Cu_2O/BiPO_4$ composites was evaluated through the degradation of pollutants under visible light irradiation in the presence of oxygen [24,25]. Different from the above conditions, we evaluated the photocatalytic activity

of $Cu_2O/BiPO_4$ composites for the co-production of H_2 and hydrocarbons under UV irradiation in the absence of oxygen. Acetic acid, propionic acid, and butyric acid were selected as electron donors, and the corresponding results were discussed in detail.

2.2.1 HAc

Figure 3 illustrated the photocatalytic activities of $BiPO_4$ and a series of prepared $Cu_2O/BiPO_4$ composites (CBP-1, CBP-3, CBP-5, CBP-7, CBP-9, CBP-10, and CBP-5) for the production of H_2 and hydrocarbons using HAc as an electron donor. As shown in Fig. 3a, regardless of the photocatalyst used, when HAc served as the electron donor, in addition to the two main gaseous products (H_2 and methane), other gaseous products were also detected in smaller amounts, including ethane, propane, and butane. This was a very interesting phenomenon, because previous literature typically reported hydrocarbons ranging from C1 to C3 [43], while the detection of butane has rarely been reported. Here, the photocatalytic performance of $BiPO_4$ and the prepared $Cu_2O/BiPO_4$ composites was evaluated based on the total production of H_2 and alkanes. The results showed that the total yield of H_2 and alkanes over all the $Cu_2O/BiPO_4$ composites prepared under various conditions was all higher than that over pure $BiPO_4$. Among them, CBP-9 exhibited the highest gas production. Compared with $BiPO_4$, the total yield of H_2 and alkanes over CBP-9 was approximately 2.49 times that over $BiPO_4$, demonstrating the excellent photocatalytic activity of CBP-9. During the photocatalytic production of H_2 and hydrocarbons, the changes in HAc were also monitored and expressed as TOC removal efficiency (Fig. 3b). As shown in Fig. 3b, the TOC removal efficiency gradually increased with irradiation time, indicating that the degradation of HAc was mainly accompanied by the production of H_2 and hydrocarbons [43,44]. After 4 h of irradiation, the TOC removal efficiency was approximately 85.71%, and the total yield of H_2 and hydrocarbons was estimated to be about 1.30 mol/mol-HAc, which was significantly higher than the results reported in the literature using Pt/TiO_2 [45] and CuO/SnO_2 [46] as photocatalysts. Furthermore, it is worth mentioning that although the present results were slightly lower than those obtained by biological processes [47], the production rate of H_2 and hydrocarbons in the photocatalytic process was much faster than that in biological processes. The observed product distribution can be rationalized by the coupling of $\cdot CH_3$ radicals generated from the photo-Kolbe decarboxylation of acetate. The dominant products CH_4 and C_2H_6 correspond to $\cdot CH_3 + \cdot H$ and $\cdot CH_3 + \cdot CH_3$ coupling, respectively. The enhanced yield over CBP-9 compared to $BiPO_4$ suggests that the heterojunction promotes the generation of $\cdot CH_3$ intermediates, although direct evidence for radical species was not obtained in this work.

To gain a deeper understanding of the photocatalytic reaction mechanisms involved in the photodegradation of acetic acid (HAc), this study proposed and discussed in detail the possible degradation pathways (as shown in Equations 1–6). The entire photocatalytic reaction process began with the ubiquitous photocatalytic water-splitting reaction. However, during photocatalytic hydrogen production, water splitting was rapidly inhibited by the continuous accumulation of hydroxyl radicals (·OH), thereby limiting further hydrogen generation. To effectively accelerate the above water-splitting

process, HAc was introduced into the photocatalytic system as an electron donor. HAc dissociated in water to form acetate ions (CH_3COO^-), which subsequently underwent the photo-Kolbe reaction to produce methyl radicals ($\cdot CH_3$) and carbon dioxide (CO_2). In this process, H_2 mainly originated from the recombination of hydrogen radicals (·H). Furthermore, the detected gaseous products methane (CH_4) and ethane (CH_3CH_3) can be attributed to the recombination of $\cdot CH_3$ radicals with ·H radicals, and the recombination of two $\cdot CH_3$ radicals, respectively. On the other hand, the formation of the liquid-phase product methanol (CH_3OH) can be explained by the photo-induced Hofer-Moest reaction, i.e., the recombination of $\cdot CH_3$ radicals with ·OH. The generated CH_3OH was further oxidized by photogenerated holes, first converting to the intermediate formaldehyde (HCHO), which was then further oxidized to the final product formic acid (HCOOH). According to the photo-Kolbe reaction mechanism, formic acid (HCCOH) can be completely converted into H_2 and CO_2, thus achieving the thorough degradation of organic compounds and the synergistic production of energy gases.

$hv + Cu_2O/BiPO_4 \rightarrow e- + h+ + H_2O \rightarrow \cdot H + \cdot OH$ (1)

$CH_3COOH \rightarrow CH_3COO^- + H^+ + h^+ \rightarrow \cdot CH_3 + CO_2$ (2)

$H + \cdot H \rightarrow H_2$ (3)

$\cdot CH_3 + \cdot H \rightarrow CH_4 \uparrow$ (4)

$\cdot CH_3 + \cdot CH_3 \rightarrow CH_3CH_3 \uparrow$ (5)

$CH_3 + \cdot OH \rightarrow CH_3OH + h^+ \rightarrow HCHO + h^+ \rightarrow HCOOH$ (6)

$HCOOH + h^+ \rightarrow H_2 \uparrow + CO_2 \uparrow$ (7)

In the photocatalytic reaction pathway proposed above, the characteristic gaseous product, including H_2, CO_2, CH_4, and CH_3CH_3, were successfully determined by gas chromatography (GC), confirming the formation pathway of the gaseous products. Meanwhile, methanol (CH_3OH) and formaldehyde (HCHO) in the liquid phase were also quantitatively analyzed using another gas chromatograph equipped with a different detector, further supporting the presence of oxygen-containing intermediates. However, due to the extremely high reactivity and very short lifetime of $\cdot CH_3$ and·OH, their direct determination under ambient conditions remained a significant technical challenge. Nevertheless, based on all the clearly detected intermediates and final products, the proposed photocatalytic degradation pathway of HAc was reasonable from both thermodynamic and kinetic perspectives.

2.2.2 HPr

The photocatalytic performance of various $Cu_2O/BiPO_4$ composites for the production of H_2 and hydrocarbons using HPr as an electron donor was shown in Fig. 3c. Compared with the results using

HAc as the electron donor, a distinct difference in the distribution of gaseous products was observed. Specifically, ethane became the most abundant component among all gaseous products, while other gases such as H_2, CH_4, propane (C_3H_8), butane (C_4H_{10}), and pentane (C_5H_{12}) coexisted as minor components. Furthermore, with increasing Cu_2O content in the $Cu_2O/BiPO_4$ composites, the total yield of ethane and butane first gradually increased, reached a maximum, and then slightly decreased. Among all the prepared composites, the CBP-9 sample still exhibited the highest gas production rate. Compared with pure $BiPO_4$, the yields of ethane and butane over CBP-9 were increased by nearly 2.27 times, again demonstrating the optimal photocatalytic activity. As can be seen from Fig. 3d, similar trends in TOC removal efficiency for HPr were observed during the photocatalytic reaction. After 4 h of irradiation, the TOC removal efficiency of HPr reached 81.63%. Meanwhile, the total yield of H_2 and hydrocarbons was calculated to be approximately 1.18 mol/mol-HPr, which was significantly higher than the results obtained in our previous study using Pt/TiO_2 as the photocatalyst [45]. However, the above yield was still lower than that reported for the photosynthetic bacteria method [47].

Similarly, a photocatalytic degradation pathway for HPr was proposed in this work using the following reaction equations (Equations 8–13). The key radical in this pathway was the $\cdot CH_2CH_3$ radical, which originated from the photo-Kolbe reaction of HPr with photogenerated holes [48,49]. Therefore, typical gaseous products such as CH_3CH_3 and butane ($CH_3CH_2CH_2CH_3$) can be regarded as the recombination of $\cdot CH_2CH_3$ radicals with ·H radicals, and the recombination of two $\cdot CH_2CH_3$ radicals, respectively. In addition, another important intermediate, ethanol (CH_3CH_2OH), was produced via the photo-induced Hofer-Moest reaction. The generated ethanol then underwent oxidation following steps similar to those of methanol. Through similar radical-radical reactions, gaseous products such as CH_4 and CH_3CH_3 can be further produced. Gaseous propane ($CH_3CH_2CH_3$) can be considered as the recombination product of $\cdot CH_2CH_3$ radicals with $\cdot CH_3$ radicals. According to our proposed photocatalytic degradation pathway, trace amounts of pentane (C_5H_{12}) were observed but could not be fully explained by the proposed pathway. A possible route involves cross-coupling of $\cdot CH_2CH_3$ and $\cdot CH_2CH_2CH_3$ radicals, although the latter is not a primary intermediate from HPr decarboxylation. Further investigation is needed to clarify its formation. In the liquid phase, various intermediates including ethanol (CH_3CH_2OH), methanol (CH_3OH), acetaldehyde (CH_3CHO), formaldehyde (HCHO), acetone (CH_3COCH_3), and acetic acid (CH_3COOH) were monitored by gas chromatography (GC). Taken together with the detection results of both gaseous products and liquid intermediates, the proposed photocatalytic degradation pathway for HPr was reasonable and credible.

$$H_2O + e^- + h^+ \rightarrow \cdot H + \cdot OH \quad (8)$$

$$CH_3CH_2COOH \rightarrow CH_3CH_2COO^- + H^+ + h^+ \rightarrow \cdot CH_2CH_3 + CO_2 \uparrow \quad (9)$$

$$\cdot H + \cdot H \rightarrow H_2 \uparrow \quad (10)$$

$$\cdot CH_2CH_3 + \cdot H \rightarrow CH_3CH_3 \uparrow \quad (11)$$

$\cdot CH_2CH_3 + \cdot CH_2CH_3 \rightarrow CH_3CH_2CH_2CH_3 \uparrow$ (12)

$\cdot CH_2CH_3 + \cdot OH \rightarrow CH_3CH_2OH + h^+ \rightarrow CH_3CHO + h^+ \rightarrow CH_3COOH$ (13)

2.2.3 HBu

The distribution of gaseous products over various $Cu_2O/BiPO_4$ composites using HBu as the electron donor was shown in Fig. 3e. As can be seen from Fig. 3e, CH_4 and propane (C_3H_8) dominated the entire photocatalytic process, while H_2 and other hydrocarbons (including ethane, butane, and pentane) were present as minor components in all gaseous products. Notably, the distribution of gaseous products obtained with HBu as the electron donor was significantly different from that obtained with HAc and HPr as electron donors. This difference can be mainly attributed to the distinct structures and reaction characteristics of the different electron donors. Consistent with the previous results, the CBP-9 sample still exhibited the highest photocatalytic efficiency among all the $Cu_2O/BiPO_4$ composites. Compared with pure $BiPO_4$, the yields of methane and propane over CBP-9 were increased by approximately 1.67 times. Meanwhile, the degradation efficiency of HBu during the photocatalytic reaction was simultaneously monitored, and the results were shown in Fig. 3f. After 4 h of irradiation, the total organic carbon (TOC) removal efficiency of HBu was 73.59%, indicating that HBu was more difficult to photocatalytically degrade than HAc and HPr. This trend was consistent with previous observations using biological processes [50]. The total yield of H_2 and hydrocarbons was calculated to be approximately 1.21 mol/mol-HBu, which was higher than the value obtained in our previous study using Cu_2O/Bi_2WO_6 as the photocatalyst [51]. Based on the above results, the CBP-9 sample can be regarded as the most efficient photocatalyst among various photocatalysts such as Pt/TiO_2 [45], CuO/SnO_2 [46], and Cu_2O/Bi_2WO_6 [51].

When HBu was used as the electron donor, more types of hydrocarbons and a greater variety of intermediates could be expected. According to the proposed photocatalytic degradation pathway for HBu (Equations 14–19), a similar photo-Kolbe reaction and a similar photo-induced Hofer-Moest reaction can occur separately. Specifically, during the photo-Kolbe reaction, characteristic radicals including $\cdot CH_2CH_2CH_3$, $\cdot CH_2CH_3$, and $\cdot CH_3$ coexisted in the reaction system. Through radical-radical recombination reactions among these different radicals, the various gaseous products observed in Fig. 3e can be reasonably explained. Moreover, C_6H_{14} was not detected under our gas chromatography (GC) conditions, possibly due to its low yield or insufficient detection sensitivity. On the other hand, in the liquid phase, a variety of representative intermediates were detected, including propanol ($CH_3CH_2CH_2OH$), isopropanol ($CH_3CHOHCH_3$), ethanol (CH_3CH_2OH), methanol (CH_3OH), propanal (CH_3CH_2CHO), acetaldehyde (CH_3CHO), formaldehyde (HCHO), acetone (CH_3COCH_3), propionic acid (CH_3CH_2COOH), and acetic acid (CH_3COOH). Based on such systematic determination of gaseous products and liquid intermediates, the proposed photocatalytic degradation pathway for HBu was likewise reasonable and credible. These results demonstrate that the carbon chain length of the VFA

substrate dictates the type of alkyl radical generated, which in turn controls the product distribution through radical coupling pathways.

$H_2O + e^- + h^+ \rightarrow \cdot H + \cdot OH$ (14)

$CH_3CH_2CH_2COOH \rightarrow CH_3CH_2CH_2COO^- + H^+ + h^+ \rightarrow \cdot CH_2CH_2CH_3 + CO_2 \uparrow$ (15)

$\cdot H + \cdot H \rightarrow H_2 \uparrow$ (16)

$\cdot CH_2CH_2CH_3 + \cdot H \rightarrow CH_3CH_2CH_3 \uparrow$ (17)

$\cdot CH_2CH_2CH_3 + \cdot CH_2CH_2CH_3 \rightarrow CH_3CH_2CH_2CH_2CH_2CH_3 \uparrow$ (18)

$\cdot CH_2CH_2CH_3 + \cdot OH \rightarrow CH_3CH_2CH_2OH + h^+ \rightarrow CH_3CH_2CHO + h^+ \rightarrow CH_3CH_2COOH$(19)

2.3 Photoluminescence (PL) spectroscopy and photoelectrochemical measurements

According to the photocatalytic H_2 and hydrocarbon production results shown in Fig. 3, CBP-9 exhibited the best activity for H_2 and hydrocarbon generation among all samples. To explore the intrinsic mechanism underlying its excellent performance, photoluminescence (PL) spectroscopy was first employed to analyze the separation efficiency of photogenerated electron–hole pairs. Generally, a higher PL emission intensity implies faster electron-hole recombination and thus lower photocatalytic activity [52]. As shown in Fig. 4a, under an excitation wavelength of 250 nm, the emission peak of pure $BiPO_4$ appeared at 440 nm, while CBP-9 showed a significantly lower PL emission intensity. This indicated that when Cu_2O (with a different band gap) was coupled with $BiPO_4$ to form a composite, the photogenerated electron-hole pairs can be more effectively transferred and separated, thereby suppressing the recombination process. This provided direct evidence for the excellent photocatalytic performance of CBP-9.

Furthermore, transient photocurrent response measurements were conducted to verify the separation and migration behavior of photogenerated charges, and the results are shown in Fig. 4b. The photocurrent of all samples increased rapidly under continuous illumination, reached a steady value, and then returned to nearly zero when the light was turned off. Pure $BiPO_4$, an n-type semiconductor, exhibited a low photocurrent density of only 0.45 $mA \cdot cm^{-2}$, attributed to the rapid recombination of photogenerated electrons and holes. In contrast, pure Cu_2O, a p-type semiconductor, showed a moderate photocurrent density of 1.57 $mA \cdot cm^{-2}$, indicating relatively more efficient charge separation. Remarkably, when an optimal content (9%) of Cu_2O was introduced into $BiPO_4$, the photocurrent density of CBP-9 significantly increased to 2.32 $mA \cdot cm^{-2}$, which was more than 5.15 times that of pure $BiPO_4$. This substantial enhancement provided strong evidence for the formation of a p-n heterojunction at the $Cu_2O/BiPO_4$ interface. Under illumination, photogenerated electrons in the conduction band of p-type

Cu_2O and holes in the valence band of n-type $BiPO_4$ can recombine at the heterojunction interface via a charge transfer process, effectively suppressing the recombination of electron–hole pairs within each individual component. Consequently, more photogenerated carriers survived and contributed to the photocurrent, leading to the observed enhancement in the CBP-9 composite.

In addition to photocurrent response, electrochemical impedance spectroscopy (EIS) measurements can further reveal the charge migration capability at the solid electrode interface, and the relevant results were shown in Fig. 4c. The photocatalytic performance of a semiconductor was closely related to its electrical conductivity, and the diameter of the semicircle in the EIS Nyquist plot reflected the charge transfer resistance. Compared with pure $BiPO_4$ and pure Cu_2O, the CBP-9 composite exhibited a significantly smaller semicircle diameter, indicating a marked reduction in charge transfer resistance at the electrolyte solution interface. This reduction in resistance facilitated more efficient migration of photogenerated charges to the electrode surface. The decreased charge transfer resistance in the CBP-9 composite can be rationalized by the formation of a p-n heterojunction. Specifically, the built-in electric field established at the $Cu_2O/BiPO_4$ interface promoted the spatial separation and directional migration of photogenerated electrons and holes, thereby reducing the overall resistance to charge transfer. The chemical interaction at the interface, as evidenced by the P-O-Cu linkages observed in the P 2p XPS spectrum, likely facilitated the formation of a robust heterojunction with efficient charge transfer pathways, consistent with the reduced charge transfer resistance observed in the EIS measurement.

Generally, the cyclic voltammetry (CV) response in the non-Faradaic potential window is dominated by double-layer capacitance. Quantifying the capacitive current within this region provides an estimate of the electrochemically active surface area (ECSA), with a larger ECSA typically reflecting a higher density of surface-active sites conducive to photocatalysis. Accordingly, CV curves of the composites were recorded in the non-Faradaic region (0.12–0.22 V vs. SCE) at scan rates of 10–60 mV s^{-1} (Fig. 4d-f). The corresponding double-layer capacitances (Cdl) of the photocatalyst surfaces, derived from the slopes of current density versus scan rate plots, are compiled in Fig. 4g. Given that Cdl is proportional to the number of surface-active sites, the highest value was observed for CBP-9 (0.121 mF.cm^{-2}), followed by Cu_2O (0.113 mF.cm^{-2})-both substantially exceeding that of $BiPO_4$ (0.106 mF.cm^{-2}). This trend confirms a richer population of active sites on CBP-9, thereby promoting its photocatalytic efficiency.

Mott-Schottky measurements were performed for $BiPO_4$ and Cu_2O in a 0.5 mol•L^{-1} Na_2SO_4 solution using an electrochemical workstation. As shown in Fig. 4h and 4i, although Cu_2O is generally regarded as a p-type semiconductor, the Mott-Schottky plot obtained under our conditions showed a positive slope, possibly due to surface states or partial oxidation. Therefore, the band edge positions derived here should be treated as approximate values. The flat-band potential derived from the plots are − 0.36 V (vs. Ag/AgCl) for $BiPO_4$ and − 0.79 V (vs. Ag/AgCl) for Cu_2O. For n-type semiconductors, the conduction band edge is typically located approximately 0.2 V below the flat-band potential. Combining the flat-band potential with the band gap energy of $BiPO_4$ (4.21 eV, Fig. 2), the conduction band potential (E_{CB}) of $BiPO_4$ versus NHE was calculated to be -0.363 eV, and the corresponding valence band potential (E_{VB})

was 3.847 eV. For Cu_2O, due to the uncertainty in the Mott-Schottky analysis, the conduction band and valence band potentials were adopted from previous reports [24], with E_{CB} = -0.793 eV and E_{VB} = 1.407 eV vs. NHE.

2.4 Stability and reusability.

The stability and reusability of photocatalytic materials are among the key evaluation indicators for their practical application. To systematically assess the performance of the CBP-9 sample in this regard, cyclic photocatalytic experiments for H_2 and hydrocarbon production were conducted (Fig. 5a). As shown in Fig. 5a, the catalytic activity of the CBP-9 sample gradually decreased with increasing number of consecutive cycles. However, after the fifth cycle under identical experimental conditions, the sample retained more than 85% of its initial photocatalytic activity. This result indicated that the CBP-9 sample exhibited good stability and reusability during the photocatalytic reactions. The potential reasons for the activity decline can be summarized as follows: physical loss of part of the sample during the recovery steps, partial dissolution of Cu_2O in the acidic medium, and the reduction of dissolved Cu^+ ions to metallic copper particles during the photocatalytic reactions. To further evaluate its stability, the CBP-9 sample after five cycles was characterized by XRD and TEM (Fig. 5b and Fig. 5c). The results showed almost no change in the crystal structure and morphology of the sample before and after the cycling reactions, fully demonstrating the excellent stability of the CBP-9 sample.

2.5 Trapping experiment.

During the photocatalytic production of H_2 and hydrocarbons, reactive species such as·OH, photogenerated electrons (e^-), and holes (h^+) play crucial roles. To elucidate the specific functions of each reactive species, researchers have widely employed scavengers for selective quenching experiments. In this study, isopropyl alcohol (IPA), silver nitrate ($AgNO_3$), and sodium oxalate ($Na_2C_2O_4$) were selected as scavengers for ·OH, e^-, and h^+, respectively [53–55]. All trapping experiments were conducted using CBP-9 as the photocatalyst, with HAc added as an electron donor. Meanwhile, a control experiment without any scavenger was performed under identical conditions for comparison. Figure 6a illustrated the effects of different scavengers on the photocatalytic production of H_2 and hydrocarbons. Compared with the control experiment, the addition of IPA had a relatively minor impact on the overall photocatalytic activity, but exhibited a distinct selective regulatory effect. The photocatalytic H_2 production was significantly inhibited, whereas the production of hydrocarbons was moderately promoted. According to our proposed reaction pathway, ·OH radicals primarily originated from the photocatalytic water-splitting reaction and were closely related to H_2 production. As a strong oxidant, ·OH radicals can participate in various redox reactions of intermediates. However, the precise mechanism by which they affected H_2 and hydrocarbon production differently remained unclear. In contrast, upon the addition of $Na_2C_2O_4$ or $AgNO_3$, the photocatalytic performance was strongly and comprehensively suppressed, with both H_2 and hydrocarbon production being markedly reduced. This phenomenon can be explained on the basis of the fundamental photocatalytic mechanism. When the

photocatalyst absorbed photons of matching energy, photogenerated e^- and h^+ were simultaneously generated in the initial stage, and together they drove the subsequent redox reactions. If either species was selectively removed by the addition of a scavenger, the electron transfer chain of the overall photocatalytic reaction was disrupted, leading to severe limitation of the overall activity for H_2 and hydrocarbon production.

2.6 Role of p-n Heterojunctions of $Cu_2O/BiPO_4$ Composites.

Figure 6b showed the characteristic electronic structure of the coupled $Cu_2O/BiPO_4$ composite and the migration pathways of photogenerated electrons and holes. According to this figure, the conduction band (CB), valence band (VB), and bandgap energy levels of Cu_2O were − 0.793 eV, 1.407 eV, and 2.20 eV, respectively [24], indicating that Cu_2O can be excited by both UV and visible light, thus possessing a broad light-responsive range. In contrast, the CB, VB, and bandgap energy levels of $BiPO_4$ were − 0.363 eV, 3.847 eV, and 4.21 eV, respectively [56]. Its wide bandgap (4.21 eV) meant that $BiPO_4$ can only be excited by UV light. In the coupled $Cu_2O/BiPO_4$ composite, numerous p-n heterojunctions can be formed at the interface between the two components. Since the CB position of Cu_2O (-0.793 eV) was more negative than that of $BiPO_4$ (-0.363 eV), photogenerated electrons can freely transfer from the CB of Cu_2O to the CB of $BiPO_4$ across the p-n heterojunctions, accumulate there, and reduce H^+ ions in the solution to H_2 gas. Meanwhile, because the VB position of $BiPO_4$ (3.847 eV) was more positive than that of Cu_2O (1.407 eV), photogenerated holes migrated in the opposite direction, transferring from the VB of $BiPO_4$ to the VB of Cu_2O and accumulating there [57], where they oxidized $RCOO^-$ anions to ·R radicals and CO_2 gas. It is well known that in a single semiconductor, most photogenerated electrons and holes recombine rapidly, thereby reducing the photonic efficiency. This phenomenon can be verified by PL and photoelectrochemical measurements. After constructing heterojunctions at the $Cu_2O/BiPO_4$ interface, the photogenerated electrons and holes became effectively separated due to proper band alignment [24,57], which was supported by photoelectrochemical measurements in Fig. 4. Furthermore, the coupled $Cu_2O/BiPO_4$ composite also extended its spectral response range, making use of both UV and visible light, as confirmed by UV-vis DRS in Fig. 2. Therefore, owing to the efficient charge carrier separation induced by the heterojunctions and the extended spectral response, the photocatalytic co-production performance of H_2 and hydrocarbons of the prepared $Cu_2O/BiPO_4$ photocatalyst was significantly enhanced, exhibiting its broad application prospects in both renewable fuel production and pollutant degradation.

3 Conclusion

In summary, a series of $Cu_2O/BiPO_4$ p-n heterojunction composites were synthesized and evaluated for the photocatalytic conversion of volatile fatty acids (VFAs: HAc, HPr, and HBu) into H_2 and C_1–C_6

alkanes. The CBP-9 composite (9 wt% Cu_2O) exhibited the highest activity among the tested samples, outperforming pristine $BiPO_4$, which is attributed to the formation of a p-n heterojunction at the $Cu_2O/BiPO_4$ interface that promotes charge separation. The distribution of gaseous products depended strongly on the type of VFA: methane and ethane dominated with HAc, ethane and butane with HPr, and methane and propane with HBu. These differences are proposed to originate from the selective coupling of alkyl radical intermediates ($\cdot CH_3$, $\cdot CH_2CH_3$, and $\cdot CH_2CH_2CH_3$) generated via the photo-Kolbe reaction. Photoluminescence, transient photocurrent, and electrochemical impedance spectroscopy results indicate that the heterojunction facilitates charge separation and migration, while trapping experiments suggest that both photogenerated electrons and holes are involved in the production of H_2 and hydrocarbons. The CBP-9 composite also showed good stability, retaining over 85% of its initial activity after five consecutive cycles with no significant changes in crystal structure or morphology. This work provides insights into how heterojunction interfacial properties influence radical intermediate coupling and product selectivity in the photocatalytic conversion of VFAs, demonstrating the potential of $Cu_2O/BiPO_4$ composites for converting biomass-derived waste streams into H_2-enriched fuel gases and expanding their application beyond conventional pollutant degradation.

Declarations

Declaration of interests

The authors declare that they have no known competing financial interests or personal relationships that could have appeared to influence the work reported in this paper.

Credit authorship contribution statement

Fenghua Chen and Xiangdong Shi: Conceptualization, Project administration, Supervision, Writing-review & editing. Qingtao Chen: Conceptualization, Methodology, Investigation, Writing-original draft. Xiaoyun Qin and Dan Luo: Conceptualization, Methodology. Xianghai Rao: Software, Validation, Data Curation.

Acknowledgements

This study was funded by Henan Province Science and Technology Programs (No.252102321042 and No. 242102230096).

References

1. M. M. Ashfaq, G. B. Tüzemen, A. Noor, Exploiting agricultural biomass via thermochemical processes for sustainable hydrogen and bioenergy: A critical review, Int. J. Hydrogen Energy 84, 1068–1084 (2024). https://doi.org/10.1016/j.ijhydene.2024.08.295.

2. Rafey, E. Ahmad, K. K. Pant, S. Upadhyayula, Transforming plastic waste into hydrogen and nanocarbon: A sustainable path to clean energy and a circular economy, Ind. Eng. Chem. Res. 64, 3651–3675 (2025). https://doi.org/10.1021/acs.iecr.4c04709.
3. OF. Aldosari, Photocatalytic water-splitting for hydrogen production using TiO_2-based catalysts: Advances, current challenges, and future perspectives, Catal. Rev. (2025). https://doi.org/10.1080/01614940.2024.2446476.
4. OF. Aldosari, I. Hussain, Unlocking the potential of TiO_2-based photocatalysts for green hydrogen energy through water-splitting: recent advances, future perspectives and techno feasibility assessment, Int. J. Hydrogen Energy 59, 958–981 (2024). https://doi.org/10.1016/j.ijhydene.2024.01.306.
5. Savateev, J. R. Zhuang, S. J. Wan, C. S. Song, S. W. Cao, J. W. Tang, Photocatalytic water splitting versus H_2 generation coupled with organic synthesis: A large critical review, Chin. J. Catal. 70, 44–114 (2025). https://doi.org/10.1016/S1872-2067(24)60216-0.
6. S. S. Mani, S. Rajendran, T. Mathew, C. S. Gopinath, A review on the recent advances in the design and structure-activity relationship of TiO_2-based photocatalysts for solar hydrogen production, Energy Adv. 3, 1472–1504 (2024). https://doi.org/10.1039/D4YA00249K.
7. S. S. Khamgaonkar, A. L. Taka, V. Maheshwari, Engineering and design of halide perovskite photoelectrochemical cells for solar-driven water splitting, Adv. Funct. Mater. 34, 2405414 (2024). https://doi.org/10.1002/adfm.202405414.
8. R. Li, F. L. Wang, F. Lv, P. F. Wang, X. Guo, J. Feng, D. Li, Y. B. Chen, Simultaneous hydrogen production and conversion of plastic wastes into valued chemicals over a Z-scheme photocatalyst, Int. J. Hydrogen Energy 51, 406–414 (2024). https://doi.org/10.1016/j.ijhydene.2023.10.069.
9. X. Y. Zhang, Z. J. Cheng, C. L. Bo, Y. X. Sun, L. Y. Piao, The photocatalytic wastewater hydrogen production process with superior performance to the overall water splitting, J. Colloid Interface Sci. 677, 189–197 (2025). https://doi.org/10.1016/j.jcis.2024.06.039.
10. C. F. Chen, C. C. Zhang Y. N. Zhang, H. J. Shang, Y. H. Shao, H. Y. Liu, C. S. Pan, Boosting H_2O_2 generation by shortening the charge migration distance in $BiPO_4$ nanocrystals, J. Colloid Interface Sci. 662, 1–10 (2024). https://doi.org/10.1016/j.jcis.2024.02.011.
11. K. J. Zhu, X. Y. Zhang, L. Wen, H. J. Chen, Y. T. Amrillah, V. Fauzia, H. Z. Dong, S. Q. Su, W. J. Luo, F. A. A. Nugroho, P. H. L. Sit, Y. H. Ng, F. F. Abdi, Electrochemical formation of $BiVO_4$/$BiPO_4$ photoanodes for enhanced selectivity toward H_2O_2 generation, Adv. Funct. Mater. 36, e17929 (2025). https://doi.org/10.1002/adfm.202517929.
12. Bouddouch, B. Akhsassi, Y. Ettahiri, L. Mllaoiy, B. Bakiz, F. Guinneton, S. Villain, A. Benlhachemi., Enhanced photocatalytic activity of $BiPO_4$ towards the photo-degradation of rhodamine B: Effect of precursor phosphates (Na_2HPO_4, KH_2PO_4, and $NH_4H_2PO_4$) on $BiPO_4$ structure, morphology and optical properties, Next Mater. 9, 100975 (2025). https://doi.org/10.1016/j.nxmate.2025.100975.

13. K. Wang, F. Yang, D. Z. Guo J. W. Wang, A comprehensive review of $BiPO_4$-based catalysts: From controlled synthesis and strategic modification to photocatalytic applications and key challenges, Inorg. Chem. Commun. 188, 116632 (2026). https://doi.org/10.1016/j.inoche.2026.116632.
14. F. S. Thomas, K. N. Aparna, A. K. N. Kumar, P. V. Suneesh, D. V. R. Kumar, Unravelling the role of ccrystal phases of $BiPO_4$ and their pproperties in the photocatalytic production of H_2O_2, Appl. Catal., A 698, 120227 (2025). https://doi.org/10.1016/j.apcata.2025.120227.
15. F. Lalrindiki, N. M. Singh, Recent advances on the synergistic effects of bismuth phosphate-based materials: Photocatalysis, photoluminescence, electrochemical properties and its biological applications, J. Ind. Eng. Chem. 146, 35–69 (2025). https://doi.org/10.1016/j.jiec.2024.11.023.
16. B. Akhsassi, A. Bouddouch, Y. Naciri, Y. Ettahiri, B. Bakiz, A. Taoufyq, S. Villain, F. Guinneton, J. R. Gavarri, A. Benlhachemi, Visible light-driven type II p-Bi_3O_4Cl/n-$BiPO_4$ heterojunction for effective photocatalytic photodegradation, Ceram. Int. 50, 32338–32352 (2024). https://doi.org/10.1016/j.ceramint.2024.06.041.
17. J. R. Wang, H. Y. Wang, C. L. Liu, z. Jiang, X. Y. Liu, Z. Y. Kang, Z. M. Hao, Q. Feng, L. J. Xu, High-performance visible-light responsive $BiPO_4$@$ZnWO_4$ photocatalyst for enhancing photodegradation characteristics, J. Sol-Gel Sci. Technol. 115, 871–884 (2024). https://doi.org/10.1007/s10971-024-06436-3.
18. Z. l. Wu, M. Fu, X. Y. Liu, J. F. Li, C. H. Wei, Y. T. Zhang, Y. J. Ning, D. W. He, Y. S. Wang, Boosting the photocathode performances of protected Cu_2O inverse opals using photonic-crystal heterostructures, Appl. Surf. Sci. 644, 158792 (2024). https://doi.org/10.1016/j.apsusc.2023.158792.
19. Sullivan, B. Zoellner P. A. Maggard, Copper(I)-based p-Type oxides for photoelectrochemical and photovoltaic solar energy conversion, Chem. Mater. 28, 5999–6016 (2016). https://doi.org/10.1021/acs.chemmater.6b00926.
20. C. Y. Toe, Z. Zheng, H. Wu, J. Scott, R. Amal, Y. H. Ng, Photocorrosion of cuprous oxide in hydrogen production: Rationalising self-oxidation or self-reduction, Angew. Chem., Int. Ed. 57, 13613–13617 (2018). https://doi.org/10.1002/anie.201807647.
21. M. Sayed, K. Z. Qi, X. H. Wu, L. Y. Zhang, H. García, J. G. Yu, Cu-based S-scheme photocatalysts, Chem. Soc. Rev. 54, 4874–4921 (2025). https://doi.org/10.1039/d4cs01091d.
22. M. Waqas, Rohma, Q. A. Sial, R. B. Ali, S. Lee, A. Kumar, H. Seo, F-incorporated Cu_2O based Z-scheme heterojunction photocathode with ALD-SnO_2 for sustainable hydrogen evolution reaction, Appl. Surf. Sci. 718, 164901 (2026). https://doi.org/10.1016/j.apsusc.2025.164901.
23. Ma, Y. J. Hua, Y. K. Cao, C. M. Jia, J. W. Li, Anchoring Cu_2O nanoparticles on g-C_3N_4 nanosheets for enhanced photocatalytic performance, Fuel 364, 131139 (2024). https://doi.org/10.1016/j.fuel.2024.131139.
24. L. Liu, L. Ding, W. J. An, S. L. Lin, J. S. Hu, Y. H. Liang, W. Q. Cui, Cu_2O NPs decorated $BiPO_4$ photocatalyst for enhanced organic contaminant degradation under visible light irradiation, RSC

Adv. 6, 29202–29209 (2016). https://doi.org/10.1039/c5ra27328e.

25. J. Q. Li, H. Yuan, Z. F. Zhu, Fabrication of Cu_2O/Au/$BiPO_4$ Z-scheme photocatalyst to improve the photocatalytic activity under solar light, J. Mol. Catal. A: Chem. 410, 133–139 (2015). https://doi.org/10.1016/j.molcata.2015.09.013.
26. A. Pugazhendhi, A. Sharma, A detailed survey of recyclable food discards for the production of alternative fuels-present and future aspects, Renewable Sustainable Energy Rev. 208, 115005 (2025). https://doi.org/10.1016/j.rser.2024.115005.
27. J. Liu, X. Wang, Z. Fan, Z. Liu, P. Xu, T. R. Sawant, G. Huang, X. Deng, J. Guo, J. Wang, M. Zhou, Valorization of agricultural residues: Challenges and opportunities in the production of bio-based materials, BioResources 20, 4798–4820 (2025). https://doi.org/10.15376/biores.20.2.Liu.
28. R. Y. Farouk, E. Mostafa, Y. Y. Wang, Evaluation of hydrogen and volatile fatty acids production system from food waste, Biomass Convers. Biorefin. 13, 5253–5259 (2023). https://doi.org/10.1007/s13399-021-02056-x.
29. E. Miynat, H. Argun, Prevention of substrate and product inhibitions by using a dilution strategy during dark fermentative hydrogen production from molasses, Int. J. Hydrogen Energy 45, 34695–34706 (2020). https://doi.org/10.1016/j.ijhydene.2020.03.118.
30. A. Ghimire, L. Frunzo, F. Pirozzi, E. Trably, R. Escudie, P. N. L. Lens, G. Esposito, A review on dark fermentative biohydrogen production from organic biomass: Process parameters and use of by-products, Appl. Energy 144, 73–95 (2015). https://doi.org/10.1016/j.apenergy.2015.01.045.
31. H. M. Ali, V. K. Tyagi, A.A. Kazmi, C. S. P. Ojiha, Biohythane production from organic fraction of municipal solid waste: Clean and green energy generation under circular economy framework, Int. J. Hydrogen Energy 95, 1080–1094 (2024). https://doi.org/10.1016/j.ijhydene.2024.11.251.
32. S. Agnihotri, D. M. Yin, A. Mahboubi, T. Sapmaz, S. Varjani, W. Qiao, D. Y. Koseoglu-lmer, M. J. Taherzadeh, A glimpse of the world of volatile fatty acids production and application: A review, Bioengineered 13, 1249–1275 (2022). https://doi.org/10.1080/21655979.2021.1996044.
33. L. M. Sanchez-Ledesma, J. A. Rodríguez-Victoria, H. Ramírez-Malule, Acidogenic fermentation of cassava wastewater: Effect of the substrate-to-microorganism ratio and temperature on volatile fatty acids production, Water 16, 3344 (2024). https://doi.org/10.3390/w16233344.
34. H. R. Wu, T. Kim, S. Ferdous, T. Scheve, Y. P. Lin, L. Valentino, M. Holtzapple, T. R. Hawkins, P. T. Bemavides, M. Urgun-Demirtas, Sustainable aviation fuel from high-strength wastewater via membrane-assisted volatile fatty acid production: experimental evaluation, techno-economic and life-cycle analyses, ACS Sustainable Chem. Eng. 12, 6990–7000 (2024). https://doi.org/10.1021/acssuschemeng.4c00167.
35. Chaudhuri, B. M. Harahap, B. K. Ahring, Membrane technologies for separating volatile fatty acids produced through arrested anaerobic digestion: A review, Clean Technol. 7, 48 (2025). https://doi.org/10.3390/cleantechnol7020048.
36. X. J. Zheng, M. Zhao, C. L. Li, Z. Zheng, L. F. Wei, F. H. Chen, H. X. Wang, P. P. Chen, X. M. Qin, Photocatalytic Co-production of hydrogen and alkanes from short chain fatty acids over Cu_2O

particle: Effects of electron donors, Int. J. Hydrogen Energy 42, 29672–29685 (2017). https://doi.org/10.1016/j.ijhydene.2017.10.083.

37. H. Ali, A. C. Guler, M. Masar, P. Urbanek, M. Urbaek, D. Skoda, P. Suly, M. Machovsky, D. Galusek I. Kuritka, Solid-state synthesis of direct Z-scheme Cu_2O/WO_3 nanocomposites with enhanced visible-light photocatalytic performance, Catalysts 11, 293 (2021). https://doi.org/10.3390/catal11020293.
38. F. Q. Liu, L. M. Wang, L. H. Xu, H. Pan D. Fan, Preparation and photocatalytic performance of hollow spherical TiO_2/Cu_2O composites, Nano 18, 2250090 (2023). https://doi.org/10.1142/S1793292022500904.
39. L. Fiermans, R. Hoogewijs, J. Vennik, Electron spectroscopy of transition metal oxide surfaces, Surf. Sci. 47, 7–40 (1975). https://doi.org/10.1016/0039-6028(75)90267-8.
40. R. Kumar, P. Raizada, A. A. P. Khan, V. H. Nguyen, Q. V. Le, S. Ghoekar, R. Selvasembian, V. Gandhi, A. Singh, P. Singh, Recent progress in emerging $Bipo_4$-based photocatalysts: synthesis, properties, modification strategies, and photocatalytic applications, J. Mater. Sci. Technol. 108, 208–225 (2022). https://doi.org/10.1016/j.jmst.2021.08.053.
41. Y. H. Lv, Y. Y. Zhu, and Y. F. Zhu, Enhanced photocatalytic performance for the $Bipo_{4-x}$ nanorod induced by surface oxygen vacancy, J. Phys. Chem. C 117, 18520–18528 (2013). https://doi.org/10.1021/jp405596e.
42. D.K. Acharya, A.K. Gurung, T.P. Yadav, G.P.Paudel, First-principle study of the structural, electronic and magnetic properties of bulks Cu_2O and CuO, J. Phys. Chem. C 128, 9693–9704 (2024). https://doi.org/10.1021/acs.jpcc.4c01102.
43. M. Uzzaman, M. Furukawa, I. Tateishi, H. Katsumata, M. F. Afrin, S. Kaneco, Photocatalytic hydrocarbon production from aqueous acetic acid using TiO_2 with simultaneous photodeposition of Cu, RSC Adv. 15, 5316–5326 (2025). https://doi.org/10.1039/d4ra08731c.
44. Y. Cao, S. N. Lou, T. Ohno, Photocatalytic reforming of acetic acid into methane over platinized Tio_2 mediated by carbonate radical anion, Mater. Lett. 347, 134552 (2023). https://doi.org/10.1016/j.matlet.2023.134552.
45. X. J. Zheng, L. F. Wei, Z. H. Zhang, Q. J. Jiang, Y. J. Wei, B. Xie, M. B. Wei, Research on photocatalytic H_2 production from acetic acid solution by Pt/Tio_2 nanoparticles under UV irradiation, Int. J. Hydrogen Energy 34, 9033–9041 (2009). https://doi.org/10.1016/j.ijhydene.2009.09.019.
46. X. J. Zheng, Y. J. Wei, L. F. Wei, B. Xie M. B. Wei, Photocatalytic H_2 production from acetic acid solution over CuO/SnO_2 nanocomposites under uv irradiation, Int. J. Hydrogen Energy 35, 11709–11718 (2010). https://doi.org/10.1016/j.ijhydene.2010.08.090.
47. X. Y. Shi, H. Q. Yu, Continuous production of hydrogen from mixed volatile fatty acids with rhodopseudomonas capsulate, Int. J. Hydrogen Energy 31, 1641–1647 (2006). https://doi.org/10.1016/j.ijhydene.2005.12.008.
48. J. Karpiel, P. Lonchambon, F. Dappozze, I Florea, D. Dragoe, C. Guillard, N. Herlin-Boime, One-step synthesis of Cu_xO_y/TiO_2 photocatalysts by laser pyrolysis for selective ethylene production from

propionic acid degradation, Nanomaterials 13, 792 (2023). https://doi.org/10.3390/nano13050792.

49. L. M. Betts, F. Dappozze, C. Guillard, Understanding the photocatalytic degradation by P25 TiO_2 of acetic acid and propionic acid in the pursuit of alkane production, Appl. Catal., A 554, 35–43 (2018). https://doi.org/10.1016/j.apcata.2018.01.011.
50. Q. P. Cheng, Z. H. Chen, F. Deng, Y. H. Liao, B. Xiao J. F. Li, Kinetic evaluation on the degradation process of anaerobic digestion fed with piggery wastewater at different OLRs, Biochem. Eng. J. 113, 123–132 (2016). https://doi.org/10.1016/j.bej.2016.06.010.
51. X. J. Zheng, C. L. Li, M. Zhao, Z. Zheng, L. F. Wei, F. H. Chen, X. L. Li, Photocatalytic degradation of butyric acid over Cu_2O/Bi_2WO_6 composites for simultaneous production of alkanes and hydrogen gas under UV irradiation, Int. J. Hydrogen Energy 42, 7917–7929 (2017). https://doi.org/10.1016/j.ijhydene.2016.12.131.
52. I. Ahmad, M. Q. Alfaifi, S. Ben Ahmed, M. M. Abduljawad, Y. A. Alassmy, S. A. Alshuhri, T. L. Tamang, Strategies for optimizing sunlight conversion in semiconductor photocatalysts: A review of experimental and theoretical insights, Int. J. Hydrogen Energy 96, 1006–1066 (2024). https://doi.org/10.1016/j.ijhydene.2024.11.388.
53. Y. Nosaka, A.Y. Nosaka, Generation and detection of reactive oxygen species in photocatalysis, Chem. Rev. 117, 11302–11336 (2017). https://doi.org/10.1016/j.surfin.2024.104033.
54. X. Xu, Y. F. Sun, Z. H. Fan, D. Q. Zhao, S. M. Xiong, Bi. Y. Zhang, S. Y. Zhou, G. T. Liu, Mechanism for $\cdot O_2^-$ and ·OH production on flowerlike $BiVO_4$ photocatalysis based on electron spin resonance, Front. Chem. 6, 64 (2018). https://doi.org/10.3389/fchem.2018.00064.
55. A. Gottuso, F. Parisi, D. Lenaz, F. Parrino, Unravelling the role of silver in addressing the nitrate radical induced photocatalytic oxidation of olefins to epoxides or carbonyl compounds, J. Photochem. Photobiol., A 457, 115871 (2024). https://doi.org/10.1016/j.jphotochem.2024.115871.
56. C. S. Pan, Y. F. Zhu, New type of $BiPO_4$ oxy-acid salt photocatalyst with high photocatalytic activity on degradation of dye, Environ. Sci. Technol. 44, 5570–5574 (2010). https://doi.org/10.1021/es101223n.
57. Y. Li, Y. W. Wang, Y. Huang, J. J. Cao, W. K. Ho, S. C. Lee, C. M. Fan, Controllable synthesis of phosphate-modified $bipo_4$ nanorods with high photocatalytic activity: Surface hydroxyl groups concentrations effects, RSC Adv. 5, 99712–99721 (2015). https://doi.org/0.1039/c5ra20189f.

Figures

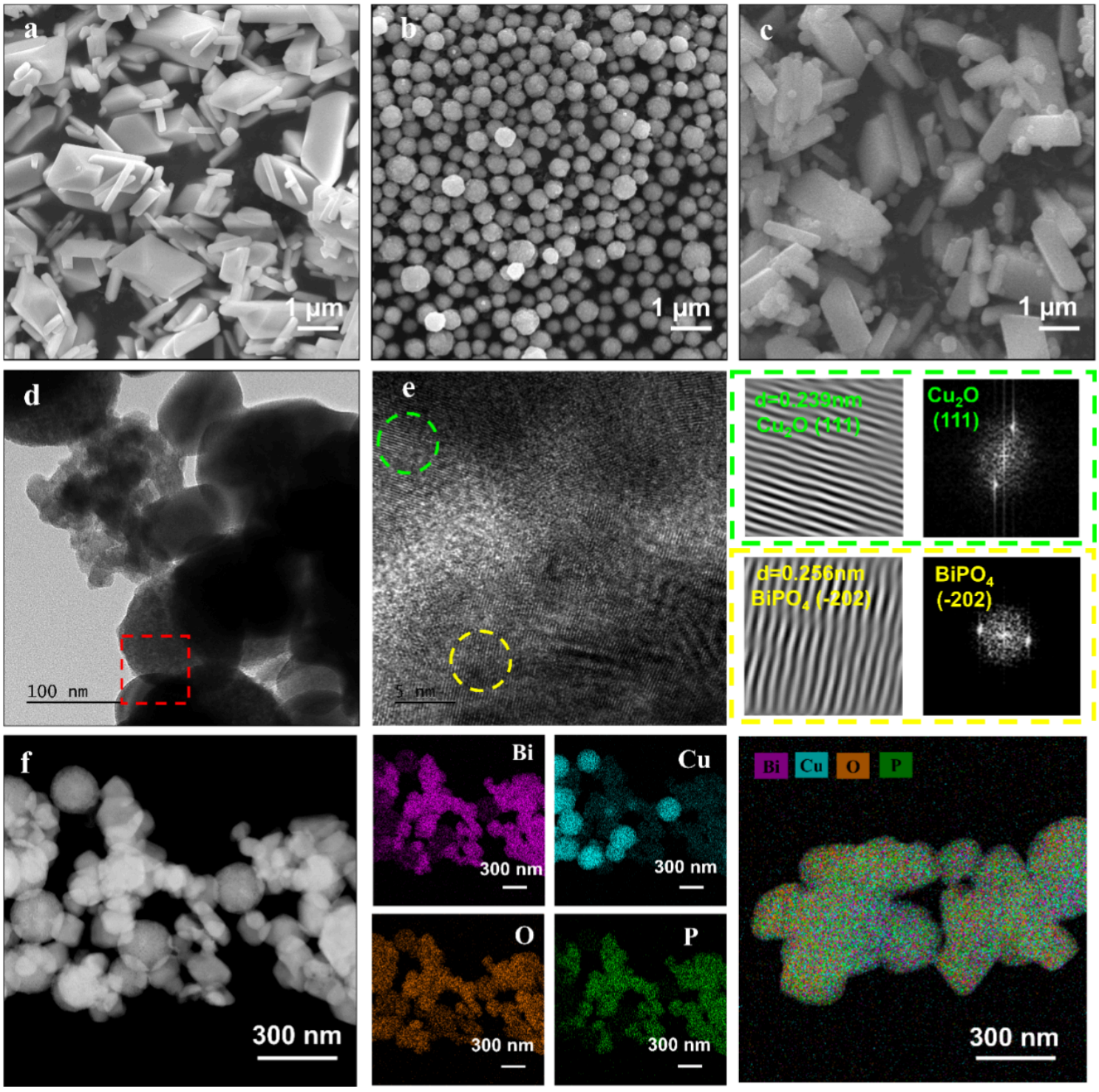


Figure 1

SEM images of (a) $BiPO_4$, (b) Cu_2O, (c) CBP-9; TEM images (d) and HRTEM images (e) of CBP-9; Elemental mapping for Bi, Cu, O and P of CBP-9

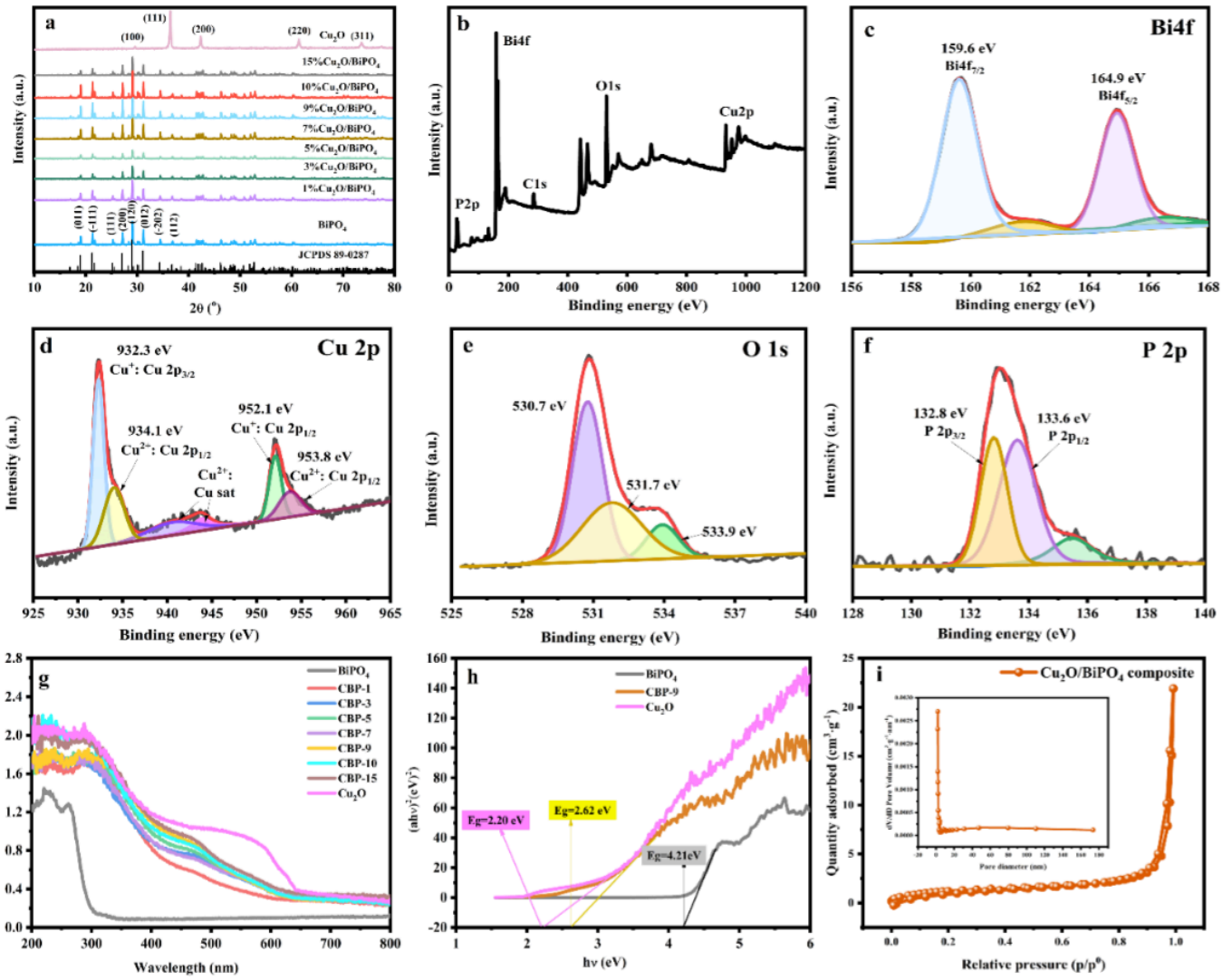


Figure 2

(a) XRD patterns of as-prepared pure Cu_2O, pure $BiPO_4$ and $Cu_2O/BiPO_4$ composites; Survey (b) and high resolution XPS spectra for Bi 4f (c), Cu 2p (d), O1s (e) and P 2p (f) of the CBP-9 sample; (g) UV-vis DRS of pure Cu_2O, pure $BiPO_4$ and various $Cu_2O/BiPO_4$ composites; (h)The Tauc plot derived from diffuse reflectance UV-Vis spectra for pure Cu_2O, pure $BiPO_4$ and CBP-9; (i) N_2 adsorption-desorption isotherms of $Cu_2O/BiPO_4$ composite

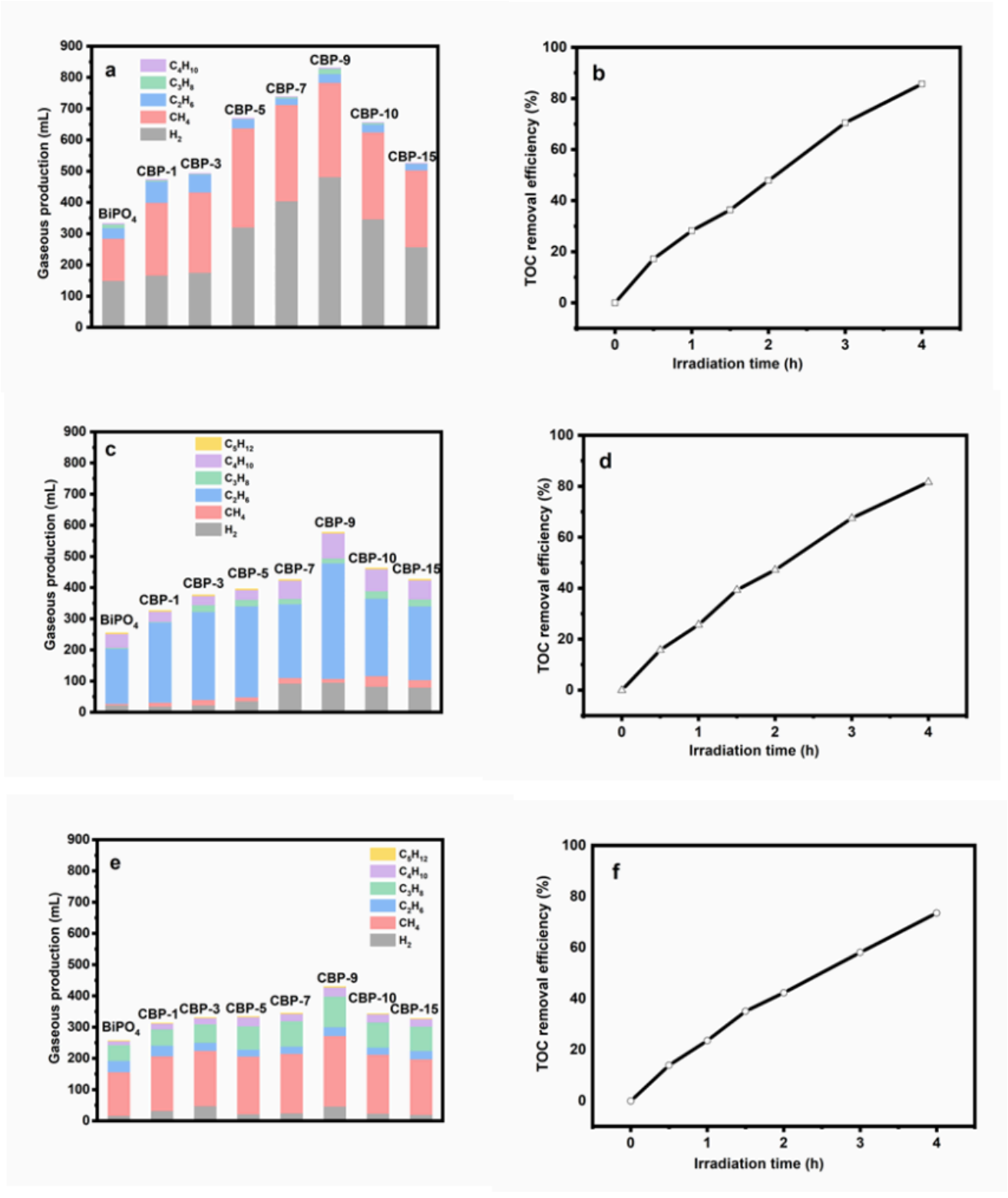


Figure 3

Comparison of photocatalytic performances for co-production of H_2 and hydrocarbons from HAc (a), HPr(c), and HBu(e) by $Cu_2O/BiPO_4$ composites and their corresponding HAc (b), HPr(d), and HBu(f) degradation curve.

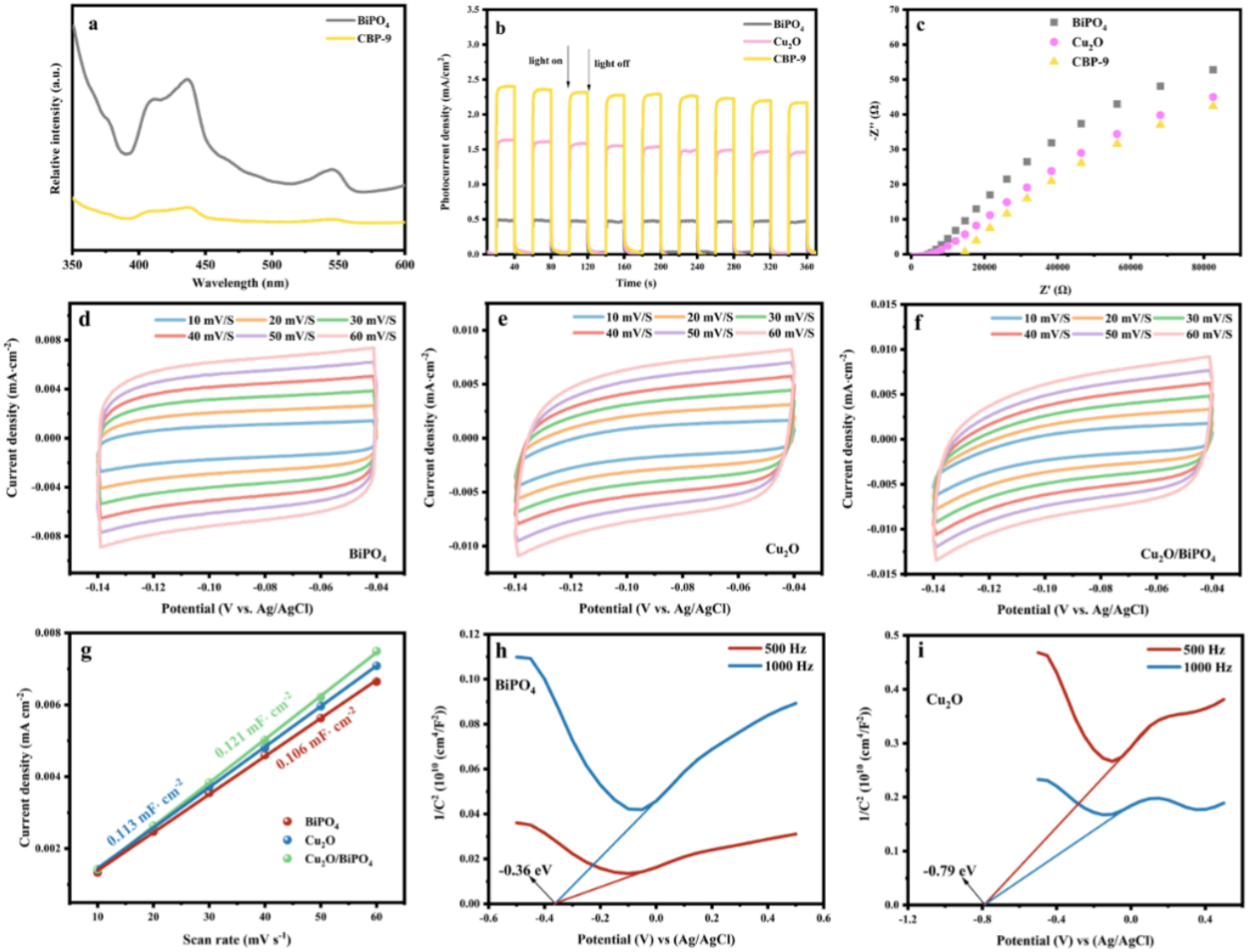


Figure 4

(a) Comparison of photoluminescence (PL) spectra with pure $BiPO_4$ and the CBP-9 sample. (b) the transient photocurrent responses, (c) EIS Nyquist plots and (d, e, f) CV curves of as-prepared pure $BiPO_4$, pure Cu_2O and the CBP-9 sample; (g) The fitting curve between the capacitance and scanning rate of $BiPO_4$, Cu_2O and the CBP-9 sample; (h, i) Mott-Schottky plots of $BiPO_4$ and Cu_2O.

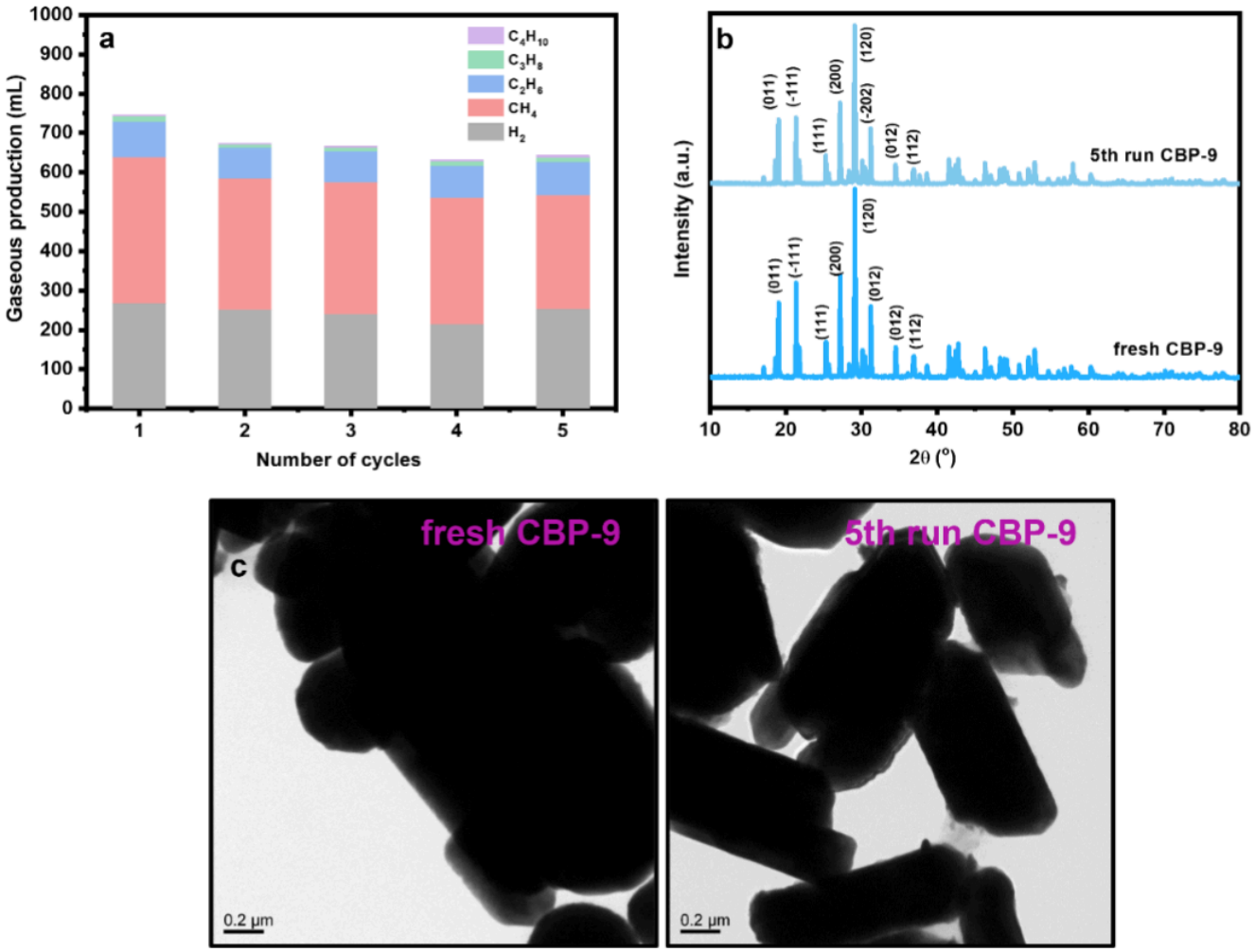


Figure 5

(a) Recycling runs of the photocatalytic production of H_2 and hydrocarbons from HAc over CBP-9 composite. (b) XRD patterns and (c) TEM images of CBP-9 sample before and after five successive runs.

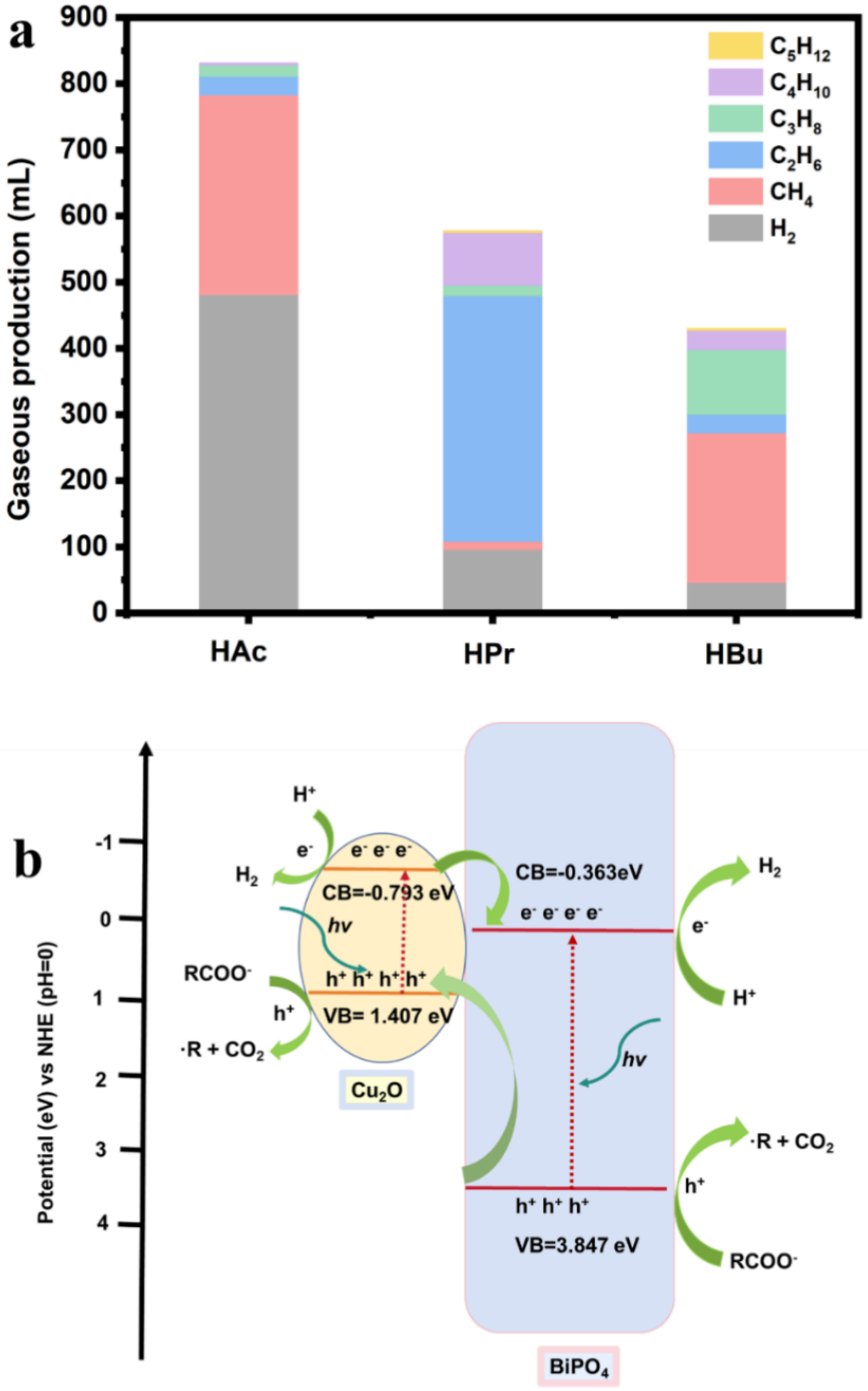


Figure 6

(a) Effects of different scavengers on photocatalytic production of H_2 and hydrocarbons over the CBP-9. (b)Schematic diagram of transfer and separation of photogenerated electrons with holes across $Cu_2O/BiPO_4$ p-n heterojunction interface during photocatalytic process.

Supplementary Files

This is a list of supplementary files associated with this preprint. Click to download.

- SupportingInformation.docx